Research Square

Preprints are preliminary reports that have not undergone peer review.
They should not be considered conclusive, used to inform clinical practice,
or referenced by the media as validated information.

A model equation for nonlinear unsteady flow through porous media

Lukas Unglehrt
Technical University of Munich
Yoshiyuki Sakai
yoshiyuki.sakai@tum.de
Technical University of Munich
Michael Manhart
Technical University of Munich

Research Article

Keywords:

Posted Date: November 6th, 2026

DOI: https://doi.org/10.21203/rs.3.rs-11442655/v1

License: This work is licensed under a Creative Commons Attribution 4.0 International License.
Read Full License

Additional Declarations: No competing interests reported.

A model equation for nonlinear unsteady flow through porous media

Lukas Unglehrt[1,2], Yoshiyuki Sakai[1*] and Michael Manhart[1]

[1]TUM School of Engineering and Design, Technical University of Munich, Arcisstr. 21, 80333 Munich, Germany.
[2]UNGLEHRT GmbH & Co. KG Bauunternehmen, Allgäuer Str. 31, 87700 Memmingen, Germany.

*Corresponding author(s). E-mail(s): yoshiyuki.sakai@tum.de;
Contributing authors: lukas.unglehrt@tum.de;
michael.manhart@tum.de;

Abstract

We propose a new model for nonlinear unsteady flow through porous media in the framework of the volume-averaged momentum equation. The drag is decomposed into the accelerative pressure drag, the viscous pressure drag, the convective pressure drag and the friction drag. The accelerative pressure drag is given in terms of the tortuosity and the macroscopic pressure gradient. The convective pressure drag is modelled by a Forchheimer-type nonlinearity. The friction drag and the viscous pressure drag are modelled together by a history term that is constructed by blending the equivalent fluid model of Pride et al. (Phys. Rev. B, 1993) with a steady laminar boundary layer scaling. The model is validated against direct numerical simulations of oscillatory flow through a hexagonal sphere pack and compared with models from the literature. The proposed model accurately represents linear flow and significantly improves the prediction of nonlinear flow at intermediate frequencies compared to the existing models. The model errors increase gradually from linear unsteady flow and nonlinear quasi-stationary flow to high-frequency nonlinear flow.

Keywords: unsteady flow, porous media, model equation, direct numerical simulation

1 Introduction

Nonlinear unsteady flow through porous media occurs in wave-induced flow through the seabed [1], coral reefs [2] or breakwaters [3]. Unsteady flow can lead to increased heat and mass transfer rates, higher mixing and more uniform velocity distributions compared to steady flow [4]. Therefore, unsteady flow through porous media is of engineering interest for systems such as cryocooler regenerators [5, 6] or chemical reactors [7, 8].

Flow through porous media is usually described in a statistical fashion due to the complex geometry of the pore space [9, p.13]. The microscopic velocity $\boldsymbol{u}$ and pressure p are averaged over a volume V containing a fluid volume V_f to form the superficial velocity

$$\langle \boldsymbol{u} \rangle_\mathrm{s} = \frac{1}{V} \int_{V_\mathrm{f}} \boldsymbol{u} \, \mathrm{d}V \tag{1}$$

and the intrinsic pressure

$$\langle p \rangle_\mathrm{i} = \frac{1}{V_\mathrm{f}} \int_{V_\mathrm{f}} p \, \mathrm{d}V \,, \tag{2}$$

which are the basic quantities of interest for flow through porous media. The governing equations for these quantities are derived from the incompressible Navier-Stokes equations by separating the variations in velocity and pressure occurring at the pore scale ℓ from those occurring at the field scale L. This can be achieved using homogenisation theory for periodic porous media [10, 11], which seeks an asymptotic description in the limit $\ell/L \to 0$, or using volume-averaging theory for general porous media [12, 13], in which a filter of width r_0 ($\ell \ll r_0 \ll L$) is applied to the equations. If the pore scale and the field scale are sufficiently well separated, the forces due to gradients of the superficial velocity are small and a local balance between the macroscopic pressure gradient, the drag and the local acceleration results

$$\rho \frac{\mathrm{d}\langle \boldsymbol{u} \rangle_\mathrm{s}}{\mathrm{d}t} = -\epsilon \boldsymbol{\nabla} \langle p \rangle_\mathrm{i} - \frac{1}{V} \int_{A_\mathrm{fs}} \tilde{p} \, \boldsymbol{n} \, \mathrm{d}A - \frac{1}{V} \int_{A_\mathrm{fs}} \boldsymbol{\tau}_\mathrm{w} \, \mathrm{d}A \,. \tag{3}$$

Here, ρ is the density, A_fs is the fluid-solid interface area, $\tilde{p} = p - \langle p \rangle_\mathrm{i}$ is the pressure deviation from the intrinsic volume average and $\boldsymbol{\tau}_\mathrm{w}$ is the wall shear stress transmitted from the fluid onto the solid. The aim of modelling is to parametrise the drag integrals in equation (3), which depend on the pore scale pressure and velocity distributions, in terms of the superficial velocity and the macroscopic pressure gradient.

Linear unsteady flow through porous media is commonly described with the equivalent fluid model [14–17], which constructs the transfer function ("dynamic permeability" or "dynamic tortuosity") between the macroscopic pressure gradient and the superficial velocity in the frequency domain based

on the asymptotic behaviour at low and high frequencies. On the other hand, models for nonlinear unsteady flow are formulated in the time domain. A simple model is the unsteady Forchheimer equation [18, 19]

$$c\,\frac{\mathrm{d}\langle \boldsymbol{u}\rangle_\mathrm{s}}{\mathrm{d}t} = -\boldsymbol{\nabla}\langle p\rangle_\mathrm{i} - a\,\langle \boldsymbol{u}\rangle_\mathrm{s} - b\,|\langle \boldsymbol{u}\rangle_\mathrm{s}|\,\langle \boldsymbol{u}\rangle_\mathrm{s}\ , \tag{4}$$

which is common in marine engineering and ocean science applications [1–3]. However, there is some uncertainty about the choice of the coefficients in the unsteady Forchheimer equation [20]: The coefficients a and b are usually determined from stationary flow experiments, but there are also frequency-dependent correlations for oscillatory flow. Moreover, for many porous media different values for a and b result in laminar or turbulent flow [20, 21]. Finally, the correct definition of the acceleration coefficient c is unclear [20]. A more refined approach has been proposed by Turo and Umnova [22] for the description of nonlinear pulse propagation, who additively combined the time domain formulation of a simplified equivalent fluid model with a quadratic Forchheimer nonlinearity. Their model can be written as

$$\begin{aligned}\rho\frac{\alpha_\infty}{\epsilon}\frac{\mathrm{d}\langle \boldsymbol{u}\rangle_\mathrm{s}}{\mathrm{d}t} = &-\boldsymbol{\nabla}\langle p\rangle_\mathrm{i} - \frac{\mu}{K}\,\langle \boldsymbol{u}\rangle_\mathrm{s} - b\,|\langle \boldsymbol{u}\rangle_\mathrm{s}|\,\langle \boldsymbol{u}\rangle_\mathrm{s} \\ &- \rho\sqrt{\nu}\frac{2\alpha_\infty}{\epsilon\Lambda}\int_{-\infty}^{t}\frac{\mathrm{d}\langle \boldsymbol{u}\rangle_\mathrm{s}}{\mathrm{d}\tau}\,\frac{1}{\sqrt{\pi(t-\tau)}}\,\mathrm{d}\tau\end{aligned} \tag{5}$$

with the kinematic viscosity ν, the porosity ϵ, the Darcy permeability K, the high-frequency limit of the dynamic tortuosity α_∞ [14], which describes the ratio $\epsilon\,\langle \boldsymbol{u}^2\rangle_\mathrm{s} / \langle \boldsymbol{u}\rangle_\mathrm{s}^2$ in potential flow, and the characteristic viscous length Λ, which describes the ratio of pore volume to surface area weighted by the square of the potential flow velocity [14]. The last term in the above equation describes the drag due to unsteady boundary layers and is analogous to the Basset history force on a moving particle [22]. A similar model, but based on the equivalent fluid model of [14–17], has been recently used by Moufid et al. [23] to investigate the nonlinear response of acoustic liners.

In our recent contribution [24], we have compared the above models based on a direct numerical simulation dataset of stationary and oscillatory flow through a hexagonal close-packed arrangement of spheres. The coefficient of the nonlinear term b in the equations (4) and (5) was determined using the stationary flow data. We found that the models (4) and (5) could not accurately represent linear flow over the entire frequency range: The unsteady Forchheimer equation showed large errors at intermediate to high frequencies and the model of Turo and Umnova [22] showed large errors at low frequencies. A model similar to the one used by Moufid et al. [23] was able to accurately represent linear flow at all frequencies. Nonlinear flow was found to be well predicted at low frequencies, but the errors increased towards high-frequency nonlinear flow, suggesting that the nonlinear drag is not adequately represented by the quadratic nonlinearity. Surprisingly, the unsteady Forchheimer

equation exhibited relatively small errors for high-frequency nonlinear flow, which could be related to a compensation of a too small damping in the acceleration term and a too large drag in the nonlinear term. In the present paper, we develop a new model for nonlinear unsteady flow which improves upon the nonlinear extension of the equivalent fluid model.

The new model builds upon the findings of our study [25], where we decomposed the drag force of direct numerical simulations of stationary and oscillatory flow through a hexagonal sphere pack according to the pressure source terms and investigated the Reynolds number scaling of these components. The volume-averaged momentum equation (3) is decomposed as

$$\rho \frac{\mathrm{d}\langle \boldsymbol{u} \rangle_{\mathrm{s}}}{\mathrm{d}t} = -\epsilon \boldsymbol{\nabla} \langle p \rangle_{\mathrm{i}} + \boldsymbol{f}_{\boldsymbol{\tau}_{\mathrm{w}}} + \boldsymbol{f}_p^{(v)} + \boldsymbol{f}_p^{(a)} + \boldsymbol{f}_p^{(c)} \,. \tag{6}$$

The friction drag is given as

$$\boldsymbol{f}_{\boldsymbol{\tau}_{\mathrm{w}}} = -\frac{1}{V} \int_{A_{\mathrm{fs}}} \boldsymbol{\tau}_{\mathrm{w}} \, \mathrm{d}A \tag{7}$$

and was observed to follow a linear scaling for small and a laminar boundary layer scaling for large Reynolds numbers. The latter observation is consistent with the wall shear stress measurements of Jolls and Hanratty [26] in stationary flow through a packed bed. The viscous pressure drag arises from the divergence of the wall shear stress and can be written as

$$\boldsymbol{f}_p^{(v)} = \frac{1}{V} \int_{A_{\mathrm{fs}}} (\boldsymbol{\nabla} \otimes \boldsymbol{\Phi})^{\mathrm{T}} \cdot \boldsymbol{\tau}_{\mathrm{w}} \, \mathrm{d}A \,, \tag{8}$$

where $\boldsymbol{\Phi}$ is an auxiliary potential describing the influence of a pressure source onto the pressure drag. Like the friction drag, the viscous pressure drag exhibits a linear scaling at small and steady laminar boundary layer scaling at large Reynolds numbers. The accelerative pressure drag is directly proportional to the macroscopic pressure gradient

$$\boldsymbol{f}_p^{(a)} = \left(\frac{1}{V} \int_{A_{\mathrm{fs}}} \boldsymbol{\Phi} \otimes \boldsymbol{n} \, \mathrm{d}A \right) \cdot \boldsymbol{\nabla} \langle p \rangle_{\mathrm{i}} = (1 - \epsilon) \, \mathsf{A} \cdot \boldsymbol{\nabla} \langle p \rangle_{\mathrm{i}} \,, \tag{9}$$

where A is the tensor of virtual inertia [27, p.403]. It is the only component that is nonzero in a potential flow and represents the resistance of the flow to acceleration. At the pore scale, the accelerative pressure guides the flow around the curved walls and prevents the fluid from accelerating normal to the wall. Finally, the convective pressure drag arises from the divergence of the convective acceleration and can be written as

$$\boldsymbol{f}_p^{(c)} = \frac{1}{V} \int_{V_{\mathrm{f}}} \boldsymbol{\Phi} \left[-\rho \, \boldsymbol{\nabla} \cdot \boldsymbol{\nabla} \cdot (\boldsymbol{u} \otimes \boldsymbol{u}) \right] \mathrm{d}V \,. \tag{10}$$

It shows a cubic scaling at small Reynolds numbers and the contribution of the time-averaged velocity field to the convective pressure drag approaches a quadratic scaling at large Reynolds numbers.

In this contribution, we construct a new model for unsteady flow through porous media based on the drag decomposition outlined above. We validate the model based on a direct numerical simulation dataset of oscillatory flow through a hexagonal close-packing of spheres and compare the predictions to models from the literature. Note that the proposed model was developed in the dissertation [28], but we aim to give a self-contained and more detailed description and validation below.

2 Derivation of the model

In this section, we derive our new model based on the decomposition of the drag outlined above. We will assume an isotropic porous medium, such that the tensor of virtual inertia is given in terms of the high-frequency limit of the dynamic tortuosity α_∞ [25]. The accelerative pressure drag can then be simplified to

$$\boldsymbol{f}_p^{(a)} = \epsilon \left(1 - \frac{1}{\alpha_\infty}\right) \boldsymbol{\nabla} \langle p \rangle_{\mathrm{i}} \,, \tag{11}$$

where α_∞ is defined in terms of the potential flow. It is related to the electrical formation factor $F = \alpha_\infty / \epsilon$ [29] for which many correlations have been proposed [30]. Hence, the accelerative pressure drag does not need to be modelled. The volume-averaged momentum equation is then given as

$$\rho \frac{\mathrm{d}\langle \boldsymbol{u} \rangle_{\mathrm{s}}}{\mathrm{d}t} = -\frac{\epsilon}{\alpha_\infty} \boldsymbol{\nabla} \langle p \rangle_{\mathrm{i}} + \underbrace{\boldsymbol{f}_{\boldsymbol{\tau}_{\mathrm{w}}} + \boldsymbol{f}_p^{(v)}}_{\text{viscous drag}} + \underbrace{\boldsymbol{f}_p^{(c)}}_{\text{convective pressure drag}} \,, \tag{12}$$

where the viscous drag, which is composed of the friction drag and the viscous pressure drag, and the convective pressure drag will be modelled separately. First, we present the parametrisations of the viscous drag and the convective pressure drag. We then derive the steady-state resistance law implied by our model, which is used to determine the model parameters in section 3.3.

2.1 Parametrisation of the friction drag and the viscous pressure drag

We start by modelling the friction drag and the viscous pressure drag. Since both have the same scaling behaviour and depend on the wall shear stress field (cf. equations 7 and 8), they are modelled together.

The model is based on the physical understanding that an impulsive change in the velocity initially leads to a potential flow with Stokes boundary layers. The boundary layers diffuse over time, weakening the velocity gradient at the wall and thus reducing the drag. The diffusion process reaches a steady state when the diffusion length $\sqrt{2\nu t}$ is of the order of the pore size, resulting in a

Stokes flow, or when the diffusion is limited by convection, resulting in steady laminar boundary layers. This leads us to consider a model of the form

$$\boldsymbol{f}_{\boldsymbol{\tau}_\mathrm{w}} + \boldsymbol{f}_p^{(v)} = -\mu \int_{-\infty}^{t} \frac{\mathrm{d}\langle \boldsymbol{u} \rangle_\mathrm{s}}{\mathrm{d}\tau}\, h_n(t-\tau, |\langle \boldsymbol{u} \rangle_\mathrm{s}(\tau)|)\, \mathrm{d}\tau\,, \tag{13}$$

where the product $\mu\, h_n(t-\tau, |\langle \boldsymbol{u} \rangle_\mathrm{s}(\tau)|)\, \mathrm{d}\langle \boldsymbol{u} \rangle_\mathrm{s}$ can be loosely interpreted as the drag at time t caused by a change $\mathrm{d}\langle \boldsymbol{u} \rangle_\mathrm{s}$ in the superficial velocity at time τ.

The kernel h_n will be constructed as a blending between two asymptotic expressions for low and high Reynolds number flow according to the method of Churchill and Usagi [31]. The blending of Churchill and Usagi [31] has been used to obtain a universally valid expression for the transient boundary layer flow over a flat plate from the Stokes and Blasius solutions [32], and we have used it to derive a model for the dissipation rate in linear unsteady flow through porous media [33]. The kernel is thus written as

$$h_n(t-\tau, |\langle \boldsymbol{u} \rangle_\mathrm{s}(\tau)|) = \left[\left(g_\mathrm{lin}(t-\tau)\right)^n + \left(g_\mathrm{nonlin}(|\langle \boldsymbol{u} \rangle_\mathrm{s}(\tau)|)\right)^n \right]^{\frac{1}{n}}\,, \tag{14}$$

where the function $g_\mathrm{lin}(t-\tau)$ represents the (unsteady) linear flow behaviour and the function $g_\mathrm{nonlin}(|\langle \boldsymbol{u} \rangle_\mathrm{s}(\tau)|)$ represents the (steady) nonlinear flow behaviour. The exponent n is generally a real number and controls the width of the Reynolds number range over which the transition between the asymptotes occurs.

Next, we formulate the limiting behaviour for linear and nonlinear flow and then choose an appropriate blending parameter n. In [24], linear flow was found to be accurately described by the equivalent fluid model of Pride et al. [16]. The friction and viscous pressure drag of the model of Pride et al. [16] can be written as the convolution integral

$$\boldsymbol{f}_\mathrm{lin} = -\mu \int_{-\infty}^{t} \frac{\mathrm{d}\langle \boldsymbol{u} \rangle_\mathrm{s}}{\mathrm{d}\tau} \underbrace{\left[\frac{\epsilon}{\alpha_\infty K} + \frac{2}{\Lambda} \frac{e^{-\frac{\nu(t-\tau)}{\Lambda^2\beta^2}}}{\sqrt{\pi\nu(t-\tau)}} - \frac{2}{\Lambda^2\beta} \mathrm{erfc}\left(\sqrt{\frac{\nu(t-\tau)}{\Lambda^2\beta^2}} \right) \right]}_{=:\, g_\mathrm{lin}(t-\tau)} \mathrm{d}\tau\,. \tag{15}$$

This expression follows from the time-domain formulation of the model of Pride et al. [16] given in [24] using integration by parts, wherein $\langle \boldsymbol{u} \rangle_\mathrm{s}(-\infty) = 0$ was assumed. The model of Pride et al. [16] has five parameters which are defined in terms of the pore geometry and the velocity fields in Stokes and potential flow: The porosity ϵ, the permeability K, the characteristic viscous length Λ, the high-frequency limit of the dynamic tortuosity α_∞ and the ratio $\beta = \alpha_0/\alpha_\infty - 1$, where α_0 is the static viscous tortuosity, which describes the ratio $\epsilon \left\langle \boldsymbol{u}^2 \right\rangle_\mathrm{s} / \langle \boldsymbol{u} \rangle_\mathrm{s}^2$ in Stokes flow. Note that the integral over the history of the superficial velocity is essential to appropriately represent the behaviour of strongly unsteady flow. This is due to the boundary layer behaviour in the small-time or high-frequency limit, where the friction and viscous pressure

drag takes the form of a semiderivative [14, 22]

$$\lim_{\frac{\nu(t-\tau)}{\beta^2\Lambda^2}\to 0}\left(\boldsymbol{f}_{\boldsymbol{\tau}_\mathrm{w}}+\boldsymbol{f}_p^{(v)}\right)=-\rho\sqrt{\nu}\frac{2}{\Lambda}\int_{-\infty}^{t}\frac{\mathrm{d}\langle\boldsymbol{u}\rangle_\mathrm{s}}{\mathrm{d}\tau}\frac{1}{\sqrt{\pi(t-\tau)}}\,\mathrm{d}\tau\,. \tag{16}$$

To comply with this asymptotic expression, we construct our nonlinear model in the form of a history term.

The nonlinear behaviour of the friction and viscous pressure drag is represented by a steady laminar boundary layer scaling. With the sphere diameter d, the friction and viscous pressure drag follow the relation [25]

$$\boldsymbol{f}_\mathrm{nonlin}=-C\rho\sqrt{\nu}\frac{|\langle\boldsymbol{u}\rangle_\mathrm{s}|^{1/2}\langle\boldsymbol{u}\rangle_\mathrm{s}}{d^{3/2}}=-C\,\frac{1}{d}\,\mu\,\langle\boldsymbol{u}\rangle_\mathrm{s}\sqrt{\frac{|\langle\boldsymbol{u}\rangle_\mathrm{s}|}{\nu d}}\,, \tag{17}$$

where the term $1/d$ can be interpreted as the surface-to-volume ratio, the square root term represents the inverse of the boundary layer thickness and C is an unknown geometry-dependent dimensionless constant. Note that the formulation of the boundary layer drag by Skjetne and Auriault [34] uses a tensor-valued coefficient. To bring the model (17) into a form compatible with the ansatz (13), we follow the same approach as in Unglehrt and Manhart [33] and rewrite the drag law as the integral of its time derivative

$$\begin{aligned}\boldsymbol{f}_\mathrm{nonlin}&=-\int_{-\infty}^{t}\frac{\mathrm{d}}{\mathrm{d}\tau}\left(C\rho\sqrt{\nu}\frac{|\langle\boldsymbol{u}\rangle_\mathrm{s}|^{1/2}\langle\boldsymbol{u}\rangle_\mathrm{s}}{d^{3/2}}\right)\mathrm{d}\tau\\&=-\mu\int_{-\infty}^{t}\frac{\mathrm{d}\langle\boldsymbol{u}\rangle_\mathrm{s}}{\mathrm{d}\tau}\underbrace{\left[\frac{3}{2}C\sqrt{\frac{|\langle\boldsymbol{u}\rangle_\mathrm{s}|}{\nu d^3}}\right]}_{=:\,g_\mathrm{nonlin}(|\langle\boldsymbol{u}\rangle_\mathrm{s}|(\tau))}\mathrm{d}\tau\,,\end{aligned} \tag{18}$$

where again $\langle\boldsymbol{u}\rangle_\mathrm{s}(-\infty)$ was assumed. It is important to note that this equation still represents a quasi-steady drag despite the integral over the history of the superficial velocity.

Finally, we determine a value of the blending parameter n based on the behaviour of weakly nonlinear flow. According to the theory of Mei and Auriault [35] for isotropic porous media, the drag at small Reynolds numbers is the sum of a linear and a cubic term in the Reynolds number, where the former represents the Darcy drag and the latter is a nonlinear correction. Considering the structure of our model (13), the kernel $h_n(t-\tau,|\langle\boldsymbol{u}\rangle_\mathrm{s}(\tau)|)$ must consist of a constant and a quadratic term with respect to the Reynolds number. At small Reynolds numbers, the kernel (14) can be expanded using the Taylor

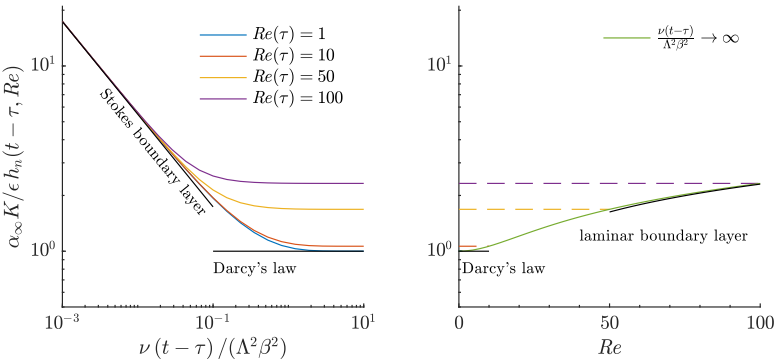


Fig. 1: Kernel $h_4(t-\tau, |\langle \boldsymbol{u} \rangle_s(\tau)|)$ as a function of the time difference $t-\tau$ for different values of the Reynolds number at time τ (left) and as a function of the Reynolds number for $\nu(t-\tau)/(\Lambda^2\beta^2) \to \infty$ (right). The material parameters are set to the values for the hexagonal sphere pack and the blending parameter is set to $n = 4$.

series of the power function [36, eq. 3.6.9] as

$$\begin{aligned} h_n(t-\tau, |\langle \boldsymbol{u} \rangle_s(\tau)|) &= g_{\text{lin}}(t-\tau) \left[1 + \left(\frac{g_{\text{nonlin}}(|\langle \boldsymbol{u} \rangle_s(\tau)|)}{g_{\text{lin}}(t-\tau)} \right)^n \right]^{\frac{1}{n}} \\ &= g_{\text{lin}}(t-\tau) \left[1 + \frac{1}{n} \left(\frac{g_{\text{nonlin}}(|\langle \boldsymbol{u} \rangle_s(\tau)|)}{g_{\text{lin}}(t-\tau)} \right)^n + \dots \right] \\ &= g_{\text{lin}}(t-\tau) \left[1 + \frac{1}{n} \left(\frac{\frac{3}{2} C/d^2}{g_{\text{lin}}(t-\tau)} \right)^n Re(\tau)^{\frac{n}{2}} + \dots \right]. \end{aligned} \tag{19}$$

If $n = 4$, the desired behaviour of the kernel at small Reynolds numbers is obtained.

Figure 1 shows the kernel as a function of the time difference $t-\tau$ and of the Reynolds number $Re(\tau) = |\langle \boldsymbol{u} \rangle_s(\tau)|\, d/\nu$. At small time differences, the kernel is independent of the Reynolds number and follows the asymptote for the Stokes boundary layer. At large time differences, the kernel becomes steady and depends only on the Reynolds number at the time when the step change $\mathrm{d}\langle \boldsymbol{u} \rangle_s$ is applied: The kernel tends to Darcy's law for small Reynolds numbers and approaches the steady laminar boundary layer expression for large Reynolds numbers

2.2 Parametrisation of the convective pressure drag

The second term that needs to be modelled is the convective pressure drag. First, we summarise what is known about the convective pressure drag. At small Reynolds numbers, the convective pressure drag has a cubic scaling

[25, 35]. Based on the resistance behaviour at large Reynolds numbers [37], the convective pressure drag can be expected to follow a quadratic scaling for large Reynolds numbers. Skjetne and Auriault [34] discussed different mechanisms that could explain this behaviour. At moderate Reynolds numbers, the quadratic scaling could come from the dissipation in free shear layers and triple decks combined with a narrowing of the flow cross-section. At large Reynolds numbers, the quadratic scaling could be caused by turbulence for which the largest scales are fixed by the pore size. Finally, we found that in unsteady flow the convective pressure drag is not always in phase with the superficial velocity and shows a hysteresis [25].

In the absence of a quantitative theory for the convective pressure drag, we model it with a Forchheimer-type quadratic nonlinearity

$$\boldsymbol{f}_p^{(c)} = -\frac{\epsilon}{\alpha_\infty}\frac{\rho B}{d}\left|\langle \boldsymbol{u}\rangle_\mathrm{s}\right|\langle \boldsymbol{u}\rangle_\mathrm{s}\ , \tag{20}$$

where B is a dimensionless coefficient. The ratio $\rho B/d$ corresponds to the Forchheimer coefficient b, but is expected to have a smaller value, since some of the nonlinear drag is represented by the viscous drag. Note that this parametrisation is not appropriate at small Reynolds numbers, where the convective pressure drag should have a Re^3 scaling.

2.3 Complete model

We now summarise the proposed model, which is the main result of our paper. The volume-averaged momentum equation is modelled as

$$\begin{aligned}\rho\frac{\mathrm{d}\langle \boldsymbol{u}\rangle_\mathrm{s}}{\mathrm{d}t} = &-\frac{\epsilon}{\alpha_\infty}\boldsymbol{\nabla}\langle p\rangle_\mathrm{i} - \mu\int_{-\infty}^{t}\frac{\mathrm{d}\langle \boldsymbol{u}\rangle_\mathrm{s}}{\mathrm{d}\tau}\,h_n(t-\tau,|\langle \boldsymbol{u}\rangle_\mathrm{s}(\tau)|)\,\mathrm{d}\tau \\ &-\frac{\epsilon}{\alpha_\infty}\frac{\rho B}{d}\left|\langle \boldsymbol{u}\rangle_\mathrm{s}\right|\langle \boldsymbol{u}\rangle_\mathrm{s}\ ,\end{aligned} \tag{21a}$$

where the kernel is given as

$$\begin{aligned}h_n(t-\tau,|\langle \boldsymbol{u}\rangle_\mathrm{s}(\tau)|) = \Bigg[&\left(\frac{\epsilon}{\alpha_\infty K} + \frac{2}{\Lambda}\frac{e^{-\frac{\nu(t-\tau)}{\Lambda^2\beta^2}}}{\sqrt{\pi\nu(t-\tau)}} - \frac{2}{\Lambda^2\beta}\mathrm{erfc}\left(\sqrt{\frac{\nu(t-\tau)}{\Lambda^2\beta^2}}\right)\right)^n \\ &+\left(\frac{3}{2}C\sqrt{\frac{|\langle \boldsymbol{u}\rangle_\mathrm{s}|}{\nu d^3}}\right)^n\Bigg]^{\frac{1}{n}}.\end{aligned} \tag{21b}$$

The porous medium enters the model through the parameters ϵ, α_∞, Λ, β, K, B and C. Note that the former five parameters are defined in terms of the geometry, the Stokes flow and the potential flow and can be taken from the literature, e.g. [38], whereas the latter two parameters have to be calibrated.

As previously discussed, we suggest to use the value $n = 4$ for the blending parameter.

In order to solve the model in time, the complete acceleration history needs to be specified. For flow started from rest at $t = 0$, the acceleration must be set to zero for all $t < 0$.

2.4 Steady-state resistance law

In this section, we will derive the steady-state resistance law implied by the model (21). Analogously to the Forchheimer equation, this explicit resistance law can be used to determine the unknown model parameters B and C from stationary flow data. In the following, we assume unidirectional flow in order to obtain a closed-form expression for the resistance law. When the viscous time scale d^2/ν is taken to be much smaller than the time scale of the superficial velocity, the time-dependent parts of the kernel (21b) are negligible and the sum of the friction and viscous pressure drag can be simplified to

$$f_{\boldsymbol{\tau}_{\mathrm{w},x}} + f_{p,x}^{(v)} = -\mu \int_{-\infty}^{t} \frac{\mathrm{d}\langle u\rangle_{\mathrm{s}}}{\mathrm{d}\tau} \left[\left(\frac{\epsilon}{\alpha_\infty K} \right)^n + \left(\frac{3}{2} C \sqrt{\frac{|\langle u\rangle_{\mathrm{s}}(\tau)|}{\nu d^3}} \right)^n \right]^{\frac{1}{n}} \mathrm{d}\tau \,. \tag{22}$$

With the initial condition $\langle u\rangle_{\mathrm{s}}(-\infty) = 0$, this integral is only a function of $\langle u\rangle_{\mathrm{s}}(t)$ and has no history dependence. This can be seen by changing the integration variable to

$$\eta = \left(\frac{3}{2} \frac{C\alpha_\infty K}{\epsilon d^2} \right)^2 \frac{\langle u\rangle_{\mathrm{s}}(\tau)\, d}{\nu} \,, \tag{23}$$

which leads to

$$\begin{aligned} \left[f_{\boldsymbol{\tau}_{\mathrm{w},x}} + f_{p,x}^{(v)} \right] \frac{d^3}{\rho\nu^2} = & -\frac{\epsilon d^2}{\alpha_\infty K} \left(\frac{3}{2} \frac{\epsilon d^2}{C\alpha_\infty K} \right)^2 \\ & \int_0^{\left(\frac{3}{2}\frac{C\alpha_\infty K}{\epsilon d^2}\right)^2 Re} \left(1 + |\eta|^{\frac{n}{2}} \right)^{\frac{1}{n}} \mathrm{d}\eta \,. \end{aligned} \tag{24}$$

Note that the equation has been nondimensionalised with the factor $d^3/(\rho\nu^2)$ and the signed Reynolds number $Re = \langle u\rangle_{\mathrm{s}}(t)\, d/\nu$ has been introduced. As is demonstrated in appendix A, the integral can be expressed in terms of Gauss' hypergeometric function ${}_2F_1(a, b;\ c;\ z)$ as

$$\begin{aligned} \left[f_{\boldsymbol{\tau}_{\mathrm{w},x}} + f_{p,x}^{(v)} \right] \frac{d^3}{\rho\nu^2} = & -\frac{\epsilon d^2}{\alpha_\infty K} Re \\ & {}_2F_1\left(-\frac{1}{n}, \frac{2}{n};\ \frac{n+2}{n};\ -\left| \left(\frac{3}{2} \frac{C\alpha_\infty K}{\epsilon d^2} \right)^2 Re \right|^{\frac{n}{2}} \right) \,. \end{aligned} \tag{25}$$

The hypergeometric function is defined as the analytic continuation of the Gauss hypergeometric series

$$ {}_2F_1(a,b;\ c;\ z) = \frac{\Gamma(c)}{\Gamma(a)\,\Gamma(b)} \sum_{k=0}^{\infty} \frac{\Gamma(a+k)\,\Gamma(b+k)}{\Gamma(c+k)} \frac{z^k}{k!} \tag{26} $$

in the complex variable z, where $\Gamma(z)$ is the gamma function [39, ch.2]. Implementations of the hypergeometric function are available in the MATLAB (`hypergeom`), Python (`scipy.special.hyp2f1`) and C programming languages (cf. Numerical Recipes [40, pp.271-273]).

Finally, the total resistance law is obtained as

$$ \begin{aligned} Hg = \frac{|\boldsymbol{\nabla}\langle p\rangle_{\mathrm{i}}|\, d^3}{\rho\nu^2} &= B\,|Re|\,Re \\ &+ \frac{d^2}{K}\,Re\,{}_2F_1\left(-\frac{1}{n}, \frac{2}{n};\ \frac{n+2}{n};\ -\left|\left(\frac{3}{2}\frac{C\alpha_\infty K}{\epsilon d^2}\right)^2 Re\right|^{\frac{n}{2}}\right) \end{aligned} \tag{27} $$

with the Hagen number Hg and the unknown parameters B and C and, possibly, n.

Figure 2 shows the above resistance law as a function of the Reynolds number. The blending parameter is set to $n = 4$ and the material parameters for a hexagonal close-packing of spheres were used (cf. section 3.3). At small Reynolds numbers, the viscous drag tends to Darcy's law while the convective pressure drag tends to zero. The viscous drag is larger than convective pressure drag for Reynolds numbers up to about 250. Due to the weak increase of the viscous drag with the Reynolds number, the total drag approaches the quadratic Reynolds number scaling very slowly. Notably, although the model parameters B and C were determined by a fit to the total resistance, the viscous drag component and the convective pressure drag component are in line with the values determined in [25] from the direct numerical simulations of Sakai and Manhart [41] (cf. also Sakai et al. [42]).

3 Methodology

3.1 Numerical method

The direct numerical simulations were conducted using the code MGLET [43]. The incompressible Navier-Stokes equations are solved on a block-structured Cartesian grid with a staggered arrangement of variables. The spatial derivatives are discretised using a second order symmetry-preserving finite volume scheme [44]. The time integration employs a third order low storage explicit Runge-Kutta scheme [45] and the projection method [46] is used to determine the pressure update in each sub-step. The no-slip and no-penetration boundary conditions on a complex geometry are imposed using a ghost cell immersed

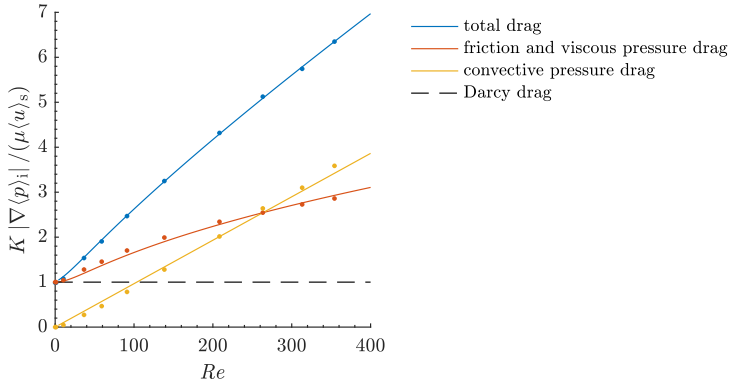


Fig. 2: Modelled steady-state resistance law (27) as a function of the Reynolds number. The drag is normalised with the Darcy drag $\mu/K\,\langle u\rangle_{\mathrm{s}}$. The symbols represent the values of the terms determined in [25] from the direct numerical simulations of stationary flow through a hexagonal sphere pack of Sakai and Manhart [41].

boundary method and flux correction procedure ensures the conservation of mass on the intersected cells [47].

3.2 Simulation dataset

We have carried out direct numerical simulations of oscillatory flow through a hexagonal close-packed array of spheres. The spheres of diameter d are arranged on a triply periodic lattice belonging to the hexagonal crystal system. The domain size is $\{L_x, L_y, L_z\} = \{2\,d, \sqrt{3}\,d, 2\sqrt{6}/3\,d\}$, which corresponds to two Cartesian unit cells stacked in the main flow direction. The grid resolution was 384 (and in some cases 768) cells per sphere diameter. The flow was driven by a pressure gradient with a sinusoidal time variation of amplitude g_x and frequency Ω. These two parameters define the two dimensionless groups determining the flow, the Womersley number $Wo = \sqrt{\Omega d^2/\nu}$ and the Hagen number $Hg = g_x d^3/(\rho\nu^2)$. The flow, including the instantaneous Reynolds number, is then a unique function of these two dimensionless numbers. We chose three Womersley numbers to cover the low- ($Wo = 10$), the medium- ($Wo = 31.62$) and the high-frequency regime ($Wo = 100$). We used the Hagen number to control whether the flow was in the linear, non-linear, transitional or turbulent regime.

Table 1 gives an overview of the flow parameters and regimes. The Reynolds number characterising the flow is calculated from the cycle-maximum superficial velocity $\max|\langle u\rangle_{\mathrm{s}}|$ obtained in the last simulated cycle, the sphere diameter d and the kinematic viscosity ν. A detailed description and analysis of the data sets can be found in [25, 48, 49].

Case	Hg	Wo	Re	number of simulated cycles	flow regime
LF1 [a]	$1.00 \cdot 10^3$	10	0.171	1.5	linear
LF2 [a]	$1.00 \cdot 10^4$	10	1.7	2.25	linear
LF3 [a]	$1.00 \cdot 10^5$	10	14.8	1.4	laminar nonlinear
LF4 [a]	$1.00 \cdot 10^6$	10	76.7	1.25	laminar nonlinear
LF5 [b]	$3.16 \cdot 10^6$	10	158	2.27	transitional
LF6 [b]	$1.00 \cdot 10^7$	10	307	1.56	turbulence-like
MF1 [a]	$1.00 \cdot 10^4$	31.6	0.857	3	linear
MF2 [a]	$1.00 \cdot 10^5$	31.6	8.57	3	linear
MF3 [a]	$3.16 \cdot 10^5$	31.6	26.9	3	laminar nonlinear
MF4 [a]	$1.00 \cdot 10^6$	31.6	73.1	3	laminar nonlinear
MF5 [b]	$3.16 \cdot 10^6$	31.6	157	6.4	transitional
MF6 [b]	$1.00 \cdot 10^7$	31.6	298	2.26	turbulence-like
HF1 [a]	$1.00 \cdot 10^5$	100	1.3	20.4	linear
HF2 [a]	$1.00 \cdot 10^6$	100	13	19.9	linear
HF3 [a]	$1.00 \cdot 10^7$	100	132	6.32	laminar nonlinear
HF4 [a]	$1.78 \cdot 10^7$	100	252	8	laminar nonlinear
HF5 [b]	$3.16 \cdot 10^7$	100	465	6	transitional
HF6 [c]	$1.00 \cdot 10^8$	100	1090	3.91	turbulence-like
HF7 [c]	$1.00 \cdot 10^9$	100	3620	10	turbulence-like

Table 1: Parameters of the simulations of oscillatory flow through a hexagonal close-packing of spheres. [a]From Unglehrt and Manhart [48]. [b]From Unglehrt and Manhart [25]. [c]From Unglehrt and Manhart [49].

Symbol	Value	Name
ϵ	0.2595	porosity
K	$1.731 \cdot 10^{-4}\, d^2$	permeability
α_0	2.657	static viscous tortuosity
α_∞	1.622	high-frequency limit of the dynamic tortuosity
Λ	$5.904 \cdot 10^{-2}\, d$	characteristic viscous length
B	55.8	convective pressure drag coefficient (defined in eq. 20)
C	141.9	boundary layer drag coefficient (defined in eq. 17)
a	μ/K	linear coefficient of the unsteady Forchheimer equation (4)
b	$88.9\, \rho/d$	nonlinear coefficient of the unsteady Forchheimer equation (4)
c	$\rho\alpha_\infty/\epsilon$	acceleration coefficient of the unsteady Forchheimer equation (4)

Table 2: Parameters for the hexagonal close-packing of spheres.

3.3 Determination of the model coefficients

Table 2 summarises the parameter values that are used to evaluate the model in the following. The parameters of the model of Pride et al. [16] are defined in terms of the Stokes flow and the potential flow. Their values for the hexagonal close-packing are given in [33] and a reasonable agreement with the values of Lee et al. [38] is observed. The coefficients B and C have no definition from first principles, and so they must be determined empirically. Here, we fit the steady resistance law (27) to the total drag of the direct numerical simulations of Sakai and Manhart [41]. As shown in figure 2, a good quality of fit is achieved and even the individual components of the drag are recovered with a good accuracy.

3.4 Discretisation of the model

In this section, we describe the discretisation of the proposed model, which is given by equation (21). The time derivative on the left hand side of the volume-averaged momentum equation is discretised by the implicit Euler method and the history term is numerically integrated using the midpoint rule

$$\begin{aligned}\rho\frac{\langle \boldsymbol{u}\rangle_{\mathrm{s}}^{k+1}-\langle \boldsymbol{u}\rangle_{\mathrm{s}}^{k}}{\Delta t} = &-\frac{\epsilon}{\alpha_\infty}\boldsymbol{\nabla}\langle p\rangle_{\mathrm{i}}^{k+1}\\ &-\frac{\epsilon}{\alpha_\infty}\frac{\rho B}{d}\left|\langle \boldsymbol{u}\rangle_{\mathrm{s}}^{k+1}\right|\langle \boldsymbol{u}\rangle_{\mathrm{s}}^{k+1}\\ &-\mu\sum_{j=-\infty}^{k}\frac{\langle \boldsymbol{u}\rangle_{\mathrm{s}}^{j+1}-\langle \boldsymbol{u}\rangle_{\mathrm{s}}^{j}}{\Delta t}\\ &\quad h_n\left(\left(k-j+\frac{1}{2}\right)\Delta t,\left|\frac{\langle \boldsymbol{u}\rangle_{\mathrm{s}}^{j}+\langle \boldsymbol{u}\rangle_{\mathrm{s}}^{j+1}}{2}\right|\right)\Delta t\,.\end{aligned} \tag{28}$$

Since the kernel $h_n(t-\tau,|\langle \boldsymbol{u}\rangle_{\mathrm{s}}(\tau)|)$ has the singularity $1/\sqrt{\pi(t-\tau)}$ for $\tau\to t$, the order of convergence of the midpoint rule is reduced to $\Delta t^{1/2}$ [50]. Consequently, the entire discretisation is half-order accurate. When evaluating the model, the time step was determined by successively halving Δt until the relative change in the root mean square superficial velocity was below a tolerance of $2.5\cdot 10^{-3}$.

The order of accuracy of the discretisation might be improved by splitting off the square root singularity from the kernel $h_n(t-\tau,|\langle \boldsymbol{u}\rangle_{\mathrm{s}}(\tau)|)$ and treating it separately, e.g. using the approach of van Hinsberg et al. [51]. The remaining integrand could be evaluated with the midpoint rule at an order of $\Delta t^{3/2}$. The computational complexity of the discretisation might be decreased by limiting the integration of the history term to a sliding time window of fixed length. The rest of the history term could be approximated by the steady-state resistance law (27).

4 Results

In this section, we will compare our proposed model to the direct numerical simulations of oscillatory flow through a hexagonal close-packing of spheres. In the *a priori* evaluation (section 4.1), the parametrisations (13) and (20) are evaluated for the simulated time series of the superficial velocity and compared to the drag components evaluated from the direct numerical simulations. In the *a posteriori* evaluation (section 4.2), the complete model (21) is evaluated for a suddenly applied sinusoidal macroscopic pressure gradient. The resulting superficial velocity is compared to the results of the direct numerical simulations.

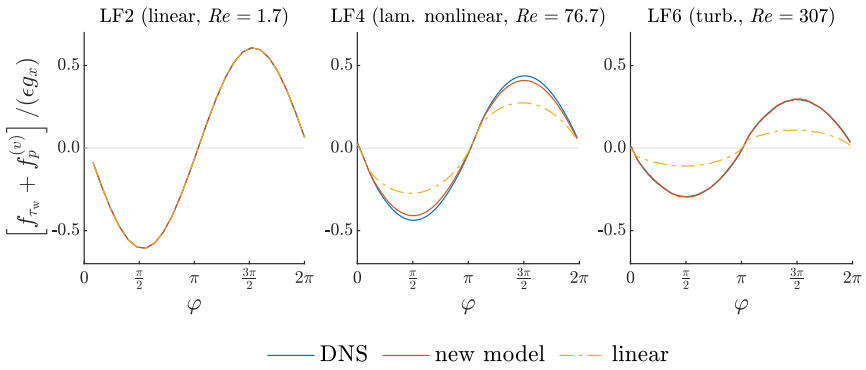


Fig. 3: *A priori* comparison of the viscous drag parametrisation (13) (solid red) to the sum of the friction and the viscous pressure drag calculated from the direct numerical simulations at $Wo = 10$ (solid blue). Also shown is the linear parametrisation (15) of Pride et al. [16] (dash-dotted yellow).

4.1 A priori evaluation

In the following we investigate the error inherent in the parametrisations of the individual drag terms. Therefore, the parametrisations are evaluated using the time series of the superficial velocity from the direct numerical simulations and the results are compared to the sum of the friction and viscous pressure drag and to the convective pressure drag, respectively, that were determined in [25].

We begin with the friction and viscous pressure drag, which are modelled together. The parametrisation is given by the equations (13) and (21b). Figures 3, 4 and 5 show the comparison between the parametrisation and the drag from the direct numerical simulations for the last simulated period at $Wo = 10$, $Wo = 31.62$ and $Wo = 100$, respectively. The drag is normalised by the amplitude ϵg_x of the body force acting on the fluid. In the linear cases LF2, MF2 and HF2, the proposed parametrisation reduces to the model of Pride et al. [16], which is also included in the graphs. For the larger Reynolds numbers, the nonlinear part of the parametrisation becomes active which can be seen from the difference to the linear model of Pride et al. [16]. In the cases LF4, LF6, MF6 and HF6 the model of Pride et al. [16] exhibits sharp kinks that are caused by sudden drops in the acceleration due to the appearance of flow separation [25]. The proposed parametrisation does not show these kinks, but introduces an appropriate amount of nonlinear drag. Overall, the parametrisation accurately represents the shape and amplitude of the drag curves despite the significantly unsteady behaviour at $Wo = 31.62$ and $Wo = 100$. For the case HF5, the amplitude of the viscous drag is somewhat overpredicted.

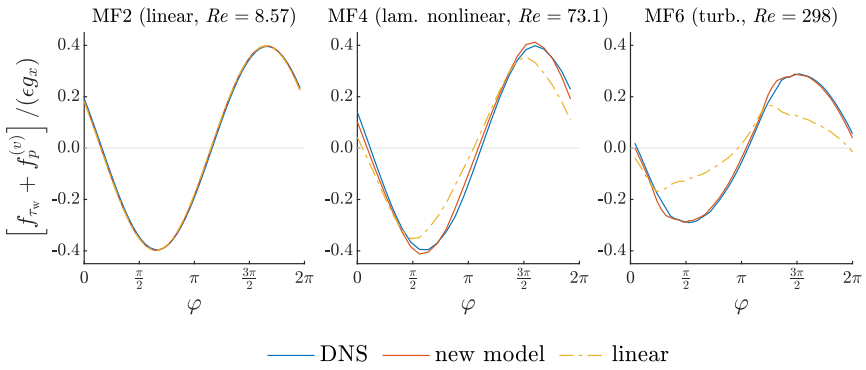


Fig. 4: *A priori* comparison of the viscous drag parametrisation (13) (solid red) to the sum of the friction and the viscous pressure drag calculated from the direct numerical simulations at $Wo = 31.62$ (solid blue). Also shown is the linear parametrisation (15) of Pride et al. [16] (dash-dotted yellow).

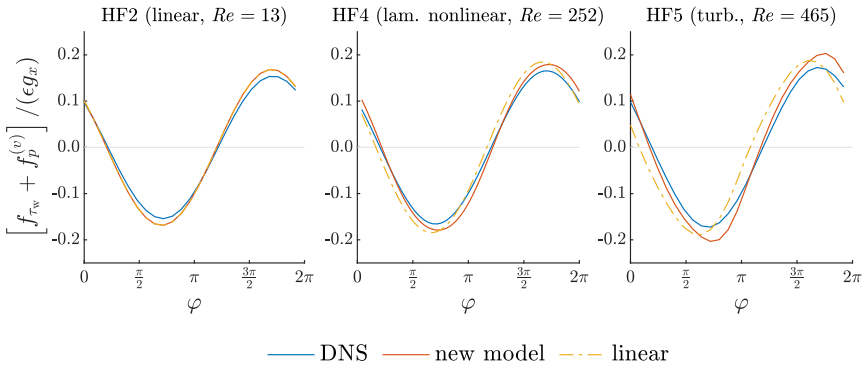


Fig. 5: *A priori* comparison of the viscous drag parametrisation (13) (solid red) to the sum of the friction and the viscous pressure drag calculated from the direct numerical simulations at $Wo = 100$ (solid blue). Also shown is the linear parametrisation (15) of Pride et al. [16] (dash-dotted yellow).

Next, we consider the convective pressure drag, which is parametrised by equation (20). Figures 6, 7 and 8 show the simulated and the modelled convective pressure drag at $Wo = 10$, $Wo = 31.62$ and $Wo = 100$, respectively. For the linear cases LF2, MF2 and HF2, the parametrisation (20) overpredicts the convective pressure drag, which is due to the quadratic dependence in the model compared to the correct cubic dependence. However, the contribution of the convective pressure drag is much smaller than the contribution of the friction and the viscous pressure drag, such that this error is not significant

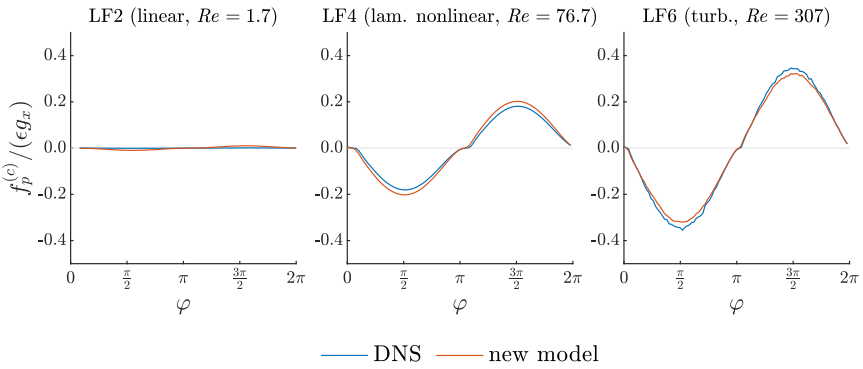


Fig. 6: *A priori* comparison of the convective pressure drag parametrisation (20) (red) to the convective pressure drag calculated from the direct numerical simulations at $Wo = 10$ (solid blue).

in the overall model. For the remaining low-frequency cases LF4 and LF6, the quadratic parametrisation works well and could probably be calibrated to exactly match the simulations. For the mid-frequency cases MF4 and MF6, the model gives a reasonable approximation, but the phase of the convective pressure drag in the case MF4 is not captured accurately. For the high-frequency cases HF4 and HF5 we observe a significant misprediction of the phase and the waveform of the convective pressure drag. In particular, the parametrisation (20) leads to saddle points that are absent from the simulations. In conclusion, the Forchheimer-type parametrisation of the convective pressure drag is appropriate at low frequencies, but its accuracy deteriorates towards high frequencies. This result was expected since the convective pressure drag in the mid- and high-frequency cases is not in phase with the superficial velocity [25].

4.2 A posteriori evaluation

In this section, we evaluate the model predictions in response to a given time series of the macroscopic pressure gradient

$$-\boldsymbol{\nabla}\langle p\rangle_{\mathrm{i}} = g_x \sin(\Omega t)\, \boldsymbol{e}_x \tag{29}$$

for different amplitudes g_x and frequencies Ω. The predicted superficial velocity is compared to the superficial velocity obtained from the direct numerical simulations. Moreover, the model accuracy is compared to the unsteady Forchheimer equation (4), to the model of Turo and Umnova [22] given by (5) and to an extension of the model of Pride et al. [16] with a quadratic nonlinearity, which can be obtained by substituting the equations (15) and $\boldsymbol{f}_p^{(c)} = -b\,|\langle \boldsymbol{u}\rangle_{\mathrm{s}}|\,\langle \boldsymbol{u}\rangle_{\mathrm{s}}$ into the volume-averaged momentum equation (12). As discussed in section 3.3, the nonlinear model coefficients have been determined by a fit to the stationary flow data.

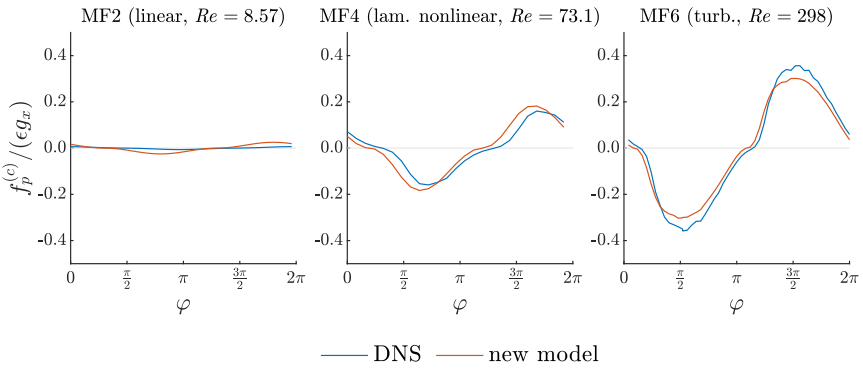


Fig. 7: *A priori* comparison of the convective pressure drag parametrisation (20) (red) to the convective pressure drag calculated from the direct numerical simulations at $Wo = 31.62$ (solid blue).

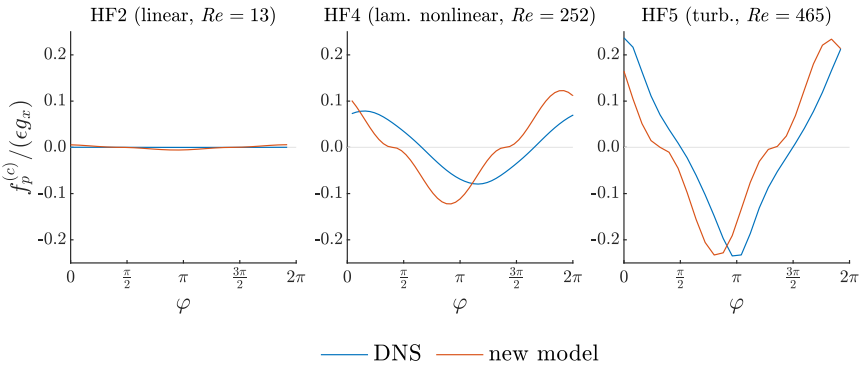


Fig. 8: *A priori* comparison of the convective pressure drag parametrisation (20) (red) to the convective pressure drag calculated from the direct numerical simulations at $Wo = 100$ (solid blue).

We measure the model error by taking the L^2 norm of the difference between the superficial velocity predicted by the model and the direct numerical simulation over the last simulated period. We normalise this error by the amplitude of the superficial velocity in the last simulated period. Table 3 lists the normalised L^2 error. For the low frequency cases, the unsteady Forchheimer equation, the modified Pride et al. [16] model and our proposed model predict the superficial velocity with an acceptable accuracy. On the other hand, the model of Turo and Umnova [22] has large prediction errors especially for the linear cases LF1–LF3. At the intermediate frequency, the proposed model has errors in the range of 0.4–4.8%, while the unsteady Forchheimer equation and

case	unsteady Forchheimer eq.	Turo & Umnova	modification of Pride et al.	new model
LF1	4.8 %	17.7 %	0.5 %	1.2 %
LF2	4.9 %	17.9 %	1.8 %	2.3 %
LF3	5.2 %	17.5 %	3.8 %	2.2 %
LF4	2.3 %	9.7 %	2.1 %	0.5 %
LF5	2.5 %	6.7 %	2.7 %	1.1 %
LF6	1.1 %	4.9 %	1.6 %	0.8 %
MF1	27.9 %	19.1 %	1.0 %	0.4 %
MF2	24.7 %	20.1 %	3.2 %	1.7 %
MF3	17.3 %	19.9 %	6.1 %	3.6 %
MF4	7.2 %	17.9 %	10.1 %	4.5 %
MF5	4.1 %	14.9 %	11.1 %	3.5 %
MF6	3.2 %	12.6 %	10.1 %	4.8 %
HF1	18.0 %	6.3 %	2.8 %	1.1 %
HF2	17.4 %	7.0 %	3.4 %	1.5 %
HF3	12.7 %	12.2 %	8.3 %	9.4 %
HF4	6.6 %	15.5 %	12.5 %	9.8 %
HF5	4.9 %	16.6 %	15.1 %	10.8 %
HF6	8.4 %	16.5 %	16.1 %	11.8 %
HF7	6.9 %	10.7 %	10.2 %	6.5 %

Table 3: Prediction errors of the different models with respect to the direct numerical simulations of oscillatory flow through a hexagonal close-packing. The prediction error is measured by the L^2 error over the last simulated period and is normalised by the amplitude of the superficial velocity. For each row, the smallest error is underlined.

the model of Turo and Umnova [22] have errors between 3.2–27.9% and 12.6–20.1%, respectively. At the highest frequency, the proposed model accurately predicts the linear cases HF1 and HF2, for which the unsteady Forchheimer equation has large errors. For the nonlinear cases HF3–HF6, the model has errors between 9.4–11.8%. This is mainly caused by the parametrisation of the convective pressure drag that, as discussed in the preceding section, does not have the correct phase and waveform. For the same cases, the model of Turo and Umnova [22] and the modified Pride et al. [16] model have errors around 15%. The unsteady Forchheiemr equation is found to have low errors for the cases HF4–HF7. This is due to an error compensation between a too small inertia and a too large drag [24].

In conclusion, the proposed model has the smallest error among all models for 12 out of the 19 simulation cases and has the second-smallest error for the remaining 7 cases. The most significant improvements over the existing models are found for flow at the intermediate frequency, where viscous, unsteady and convective effects are of comparable importance. The largest errors of the proposed model are found for nonlinear flow at the highest frequency (HF3–HF6).

5 Conclusion

We have proposed a new model for nonlinear unsteady flow through porous media, which is based on the decomposition of the drag in the volume-averaged momentum equation in [25]. The drag is represented by three contributions: The accelerative pressure drag is available in closed form and does not need to be modelled. The friction and the viscous pressure drag are parametrised together and are modelled by blending a drag expression from the equivalent fluid model of Pride et al. [16] for small Reynolds with an expression for steady laminar boundary layers for large Reynolds numbers. The convective pressure drag is modelled by a quadratic Forchheimer-type nonlinearity.

The model was validated against direct numerical simulations of oscillatory flow through a hexagonal close-packing of spheres. Given the simulated superficial velocity, the parametrisation of the friction and viscous pressure drag can reproduce the values from the simulation with good accuracy. In contrast, the parametrisation of the convective pressure drag overestimates the drag at small Reynolds numbers and cannot reproduce the correct phase of the convective pressure drag at high frequencies.

The model predictions were compared to the unsteady Forchheimer equation, the model of Turo and Umnova [22] and a nonlinear extension of the model of Pride et al. [16] similar to the one employed by Moufid et al. [23]. The proposed model can accurately represent low- and medium-frequency flow as well as high-frequency linear flow. Its largest errors are for nonlinear flow at high frequencies, where the unsteady Forchheimer equation is more accurate. Compared to the existing models, the proposed model results in significantly improved predictions for flow at intermediate frequencies.

Future work should investigate the proposed model equation for different porous medium geometries. In particular, the validity of the laminar boundary layer scaling of the friction and viscous pressure drag needs to be confirmed. Furthermore, the understanding of the model coefficients B and C, which have been defined based on scaling arguments, could be improved by understanding their dependence on the pore geometry. The proposed model could be further improved by developing a more accurate parametrisation for the convective pressure drag. Moreover, the boundary layers may be strongly affected by the turbulence in the core flow beyond Reynolds numbers in the order of magnitude of 10^3 to 10^4. We expect that a different parametrisation of the friction and the viscous pressure drag would be necessary in this regime. Due to the rapid time scales introduced by turbulent fluctuations, such a model could probably be formulated without a history term. Finally, we note that the sum of the friction and the viscous pressure drag is explicitly available in the proposed model. As the heat and mass transfer rate at the wall are often correlated with the wall shear stress, it appears promising to use our model as a basis for the description of scalar transport processes in porous media.

Appendix A Drag integral in terms of the Gauss hypergeometric function

In this appendix, the integral

$$\int_0^u \left(1 + |s|^{\frac{n}{2}}\right)^{\frac{1}{n}} \,\mathrm{d}s \tag{A1}$$

is evaluated in terms of Gauss' hypergeometric function. Following Abramowitz and Stegun [36, eq. 15.3.1], the hypergeometric function has the following integral representation

$${}_2F_1(a, b;\ c;\ z) = \frac{\Gamma(c)}{\Gamma(b)\Gamma(c-b)} \int_0^1 t^{b-1}(1-t)^{c-b-1}(1-tz)^{-a}\,\mathrm{d}t\,. \tag{A2}$$

The right arguments of the hypergeometric function were guessed based on symbolic integrations for small integer values of n using the WolframAlpha computer algebra system. Inserting these arguments, the following identity is obtained

$${}_2F_1\left(-\frac{1}{n}, \frac{2}{n};\ \frac{n+2}{n};\ -|u|^{\frac{n}{2}}\right) = \frac{2}{n}\int_0^1 t^{\frac{2}{n}-1}\left(1 + t\,|u|^{\frac{n}{2}}\right)^{\frac{1}{n}}\,\mathrm{d}t\,. \tag{A3}$$

Note that t can be pulled into the absolute value as it ranges from 0 to 1. Using the substitution $s = u\,t^{2/n}$ with $\mathrm{d}s = \frac{2}{n}\,u\,t^{2/n-1}$, the integral can be rewritten as

$${}_2F_1\left(-\frac{1}{n}, \frac{2}{n};\ \frac{n+2}{n};\ -|u|^{\frac{n}{2}}\right) = \frac{1}{u}\int_0^u \left(1 + |s|^{\frac{n}{2}}\right)^{\frac{1}{n}}\,\mathrm{d}s\,. \tag{A4}$$

The final result is obtained after multiplication by u.

Declarations

Funding. The authors gratefully acknowledge the financial support of the Deutsche Forschungsgemeinschaft (DFG, German Research Foundation) under grant no. MA2062/13-1. Computing time was granted by the Leibniz Supercomputing Centre on its Linux-Cluster.

Competing Interests. The authors have no relevant financial or non-financial interests to disclose.

Author Contributions. L.U. developed the model, conducted the model validation and drafted the manuscript. M.M. and Y.S. contributed to writing the manuscript.

Data Availability. The time series of the superficial velocity and kinetic energy for the simulations LF1–LF4, MF1–MF4 and HF1–HF4 are provided as a supplement to [48]. The time series of the superficial velocity and kinetic

energy for the simulations LF5, LF6, MF5, MF6 and HF5 are provided as a supplement to [25]. The time series of the superficial velocity and kinetic energy for the simulations HF6 and HF7 are provided as a supplement to [24].

References

[1] Gu, Z., Wang, H.: Gravity waves over porous bottoms. Coastal Engineering **15**(5-6), 497–524 (1991) https://doi.org/10.1016/0378-3839(91)90025-C

[2] Lowe, R.J., Shavit, U., Falter, J.L., Koseff, J.R., Monismith, S.G.: Modeling flow in coral communities with and without waves: A synthesis of porous media and canopy flow approaches. Limnology and Oceanography **53**(6), 2668–2680 (2008) https://doi.org/10.4319/lo.2008.53.6.2668

[3] van Gent, M.R.A.: The modelling of wave action on and in coastal structures. Coastal Engineering **22**(3-4), 311–339 (1994) https://doi.org/10.1016/0378-3839(94)90041-8

[4] Ni, X., Mackley, M.R., Harvey, A.P., Stonestreet, P., Baird, M.H.I., Rama Rao, N.V.: Mixing Through Oscillations and Pulsations—A Guide to Achieving Process Enhancements in the Chemical and Process Industries. Chemical Engineering Research and Design **81**(3), 373–383 (2003) https://doi.org/10.1205/02638760360596928

[5] Cha, J.J.: Hydrodynamic Parameters of Micro Porous Media for Steady and Oscillatory Flow: Application to Cryocooler Regenerators. PhD thesis, Georgia Institute of Technology, Atlanta, Georgia (July 2007)

[6] Pathak, M.G.: Periodic flow physics in porous media of regenerative cryocoolers. PhD thesis, Georgia Institute of Technology, Atlanta, Georgia (May 2013)

[7] Crittenden, B.D., Lau, A., Brinkmann, T., Field, R.W.: Oscillatory flow and axial dispersion in packed beds of spheres. Chemical Engineering Science **60**(1), 111–122 (2005) https://doi.org/10.1016/j.ces.2004.07.061

[8] Zagoruiko, A.N., Bobrova, L., Vernikovskaya, N., Zazhigalov, S.: Unsteady-state operation of reactors with fixed catalyst beds. Reviews in Chemical Engineering **37**(1), 193–225 (2021) https://doi.org/10.1515/revce-2019-0017

[9] Bear, J.: Dynamics of Fluids in Porous Media. Dover Publications, New York, NY (2013)

[10] Ene, H., Sanchez-Palencia, E.: Equations et phénomènes de surface pour l'écoulement dans un milieu poreux. Journal de Mécanique **14**(1), 73–108

(1975)

[11] Lévy, T.: Introduction to homogenization theory. In: Sanchez-Palencia, E., Zaoui, A. (eds.) Homogenization Techniques for Composite Media. Lecture Notes in Physics, vol. 272, pp. 63–74. Springer Berlin Heidelberg, Berlin, Heidelberg (1987). https://doi.org/10.1007/3-540-17616-0_5

[12] Hassanizadeh, S.M., Gray, W.G.: High velocity flow in porous media. Transport in Porous Media **2**(6), 521–531 (1987) https://doi.org/10.1007/BF00192152

[13] Whitaker, S.: The Forchheimer equation: A theoretical development. Transport in Porous Media **25**(1), 27–61 (1996) https://doi.org/10.1007/BF00141261

[14] Johnson, D.L., Koplik, J., Dashen, R.: Theory of dynamic permeability and tortuosity in fluid-saturated porous media. Journal of Fluid Mechanics **176**, 379–402 (1987) https://doi.org/10.1017/S0022112087000727

[15] Champoux, Y., Allard, J.-F.: Dynamic tortuosity and bulk modulus in air-saturated porous media. Journal of Applied Physics **70**(4), 1975–1979 (1991) https://doi.org/10.1063/1.349482

[16] Pride, S.R., Morgan, F.D., Gangi, A.F.: Drag forces of porous-medium acoustics. Physical Review B **47**(9), 4964–4978 (1993) https://doi.org/10.1103/PhysRevB.47.4964

[17] Lafarge, D., Lemarinier, P., Allard, J.F., Tarnow, V.: Dynamic compressibility of air in porous structures at audible frequencies. The Journal of the Acoustical Society of America **102**(4), 1995–2006 (1997) https://doi.org/10.1121/1.419690

[18] Polubarinova-Kochina, P.I.: Theory of Ground Water Movement. Princeton University Press, Princeton, NJ (1962)

[19] Sollitt, C.K., Cross, R.H.: Wave Transmission through Permeable Breakwaters. In: Coastal Engineering 1972, pp. 1827–1846. American Society of Civil Engineers, Vancouver, British Columbia (1972). https://doi.org/10.1061/9780872620490.106

[20] Burcharth, H.F., Andersen, O.K.: On the one-dimensional steady and unsteady porous flow equations. Coastal Engineering **24**(3-4), 233–257 (1995) https://doi.org/10.1016/0378-3839(94)00025-S

[21] Fand, R.M., Kim, B.Y.K., Lam, A.C.C., Phan, R.T.: Resistance to the Flow of Fluids Through Simple and Complex Porous Media Whose Matrices Are Composed of Randomly Packed Spheres. Journal of Fluids

Engineering **109**(3), 268–273 (1987) https://doi.org/10.1115/1.3242658

[22] Turo, D., Umnova, O.: Influence of Forchheimer's nonlinearity and transient effects on pulse propagation in air saturated rigid granular materials. The Journal of the Acoustical Society of America **134**(6), 4763–4774 (2013) https://doi.org/10.1121/1.4824969

[23] Moufid, I., Roncen, R., Matignon, D., Piot, E.: Time-domain simulation of the acoustic nonlinear response of acoustic liners at high sound pressure level. Nonlinear Dynamics (2024) https://doi.org/10.1007/s11071-023-09219-7

[24] Unglehrt, L., Manhart, M.: Assessment of Models for Nonlinear Oscillatory Flow Through a Hexagonal Sphere Pack. Transport in Porous Media **151**(10-11), 2183–2213 (2024) https://doi.org/10.1007/s11242-024-02110-y

[25] Unglehrt, L., Manhart, M.: Decomposition of the drag force in steady and oscillatory flow through a hexagonal sphere pack. Journal of Fluid Mechanics **974**, 32 (2023) https://doi.org/10.1017/jfm.2023.798

[26] Jolls, K.R., Hanratty, T.J.: Use of electrochemical techniques to study mass transfer rates and local skin friction to a sphere in a dumped bed. AIChE Journal **15**(2), 199–205 (1969) https://doi.org/10.1002/aic.690150214

[27] Batchelor, G.K.: An Introduction to Fluid Dynamics. Cambridge University Press, Cambridge (2000). https://doi.org/10.1017/CBO9780511800955

[28] Unglehrt, L.: Oscillatory flow through porous media. PhD thesis, Technische Universität München (2024). https://nbn-resolving.de/urn/resolver.pl?urn:nbn:de:bvb:91-diss-20240422-1729913-1-2 Accessed 2024-06-21

[29] Chapman, A.M., Higdon, J.J.L.: Oscillatory Stokes flow in periodic porous media. Physics of Fluids A: Fluid Dynamics **4**(10), 2099–2116 (1992) https://doi.org/10.1063/1.858507

[30] Mabrouk, W.M., Soliman, K.S.: A numerical technique for an accurate determination of formation resistivity factor using FR-RO overlays method. Arabian Journal of Geosciences **8**(3), 1291–1297 (2015) https://doi.org/10.1007/s12517-014-1311-4

[31] Churchill, S.W., Usagi, R.: A general expression for the correlation of rates of transfer and other phenomena. AIChE Journal **18**(6), 1121–1128 (1972) https://doi.org/10.1002/aic.690180606

[32] Muzychka, Y.S., Yovanovich, M.M.: Unsteady Viscous Flows and Stokes's First Problem. In: Fluids Engineering. ASME International Mechanical Engineering Congress and Exposition, pp. 89–99. ASMEDC, Chicago, IL (2006). https://doi.org/10.1115/IMECE2006-14301

[33] Unglehrt, L., Manhart, M.: A model for the dissipation rate in linear unsteady flow through porous media. Journal of Fluid Mechanics **975**, 42 (2023) https://doi.org/10.1017/jfm.2023.889

[34] Skjetne, E., Auriault, J.-L.: High-Velocity Laminar and Turbulent Flow in Porous Media. Transport in Porous Media **36**(2), 131–147 (1999) https://doi.org/10.1023/A:1006582211517

[35] Mei, C.C., Auriault, J.-L.: The effect of weak inertia on flow through a porous medium. Journal of Fluid Mechanics **222**, 647–663 (1991) https://doi.org/10.1017/S0022112091001258

[36] Abramowitz, M., Stegun, I.A.: Handbook of Mathematical Functions with Formulas, Graphs, and Mathematical Tables, 10th corr. edn. Applied Mathematics Series (Washington, D.C.), vol. 55. U.S. Department of Commerce, Washington, D.C. (1972)

[37] Macdonald, I.F., El-Sayed, M.S., Mow, K., Dullien, F.A.L.: Flow through Porous Media-the Ergun Equation Revisited. Industrial & Engineering Chemistry Fundamentals **18**(3), 199–208 (1979) https://doi.org/10.1021/i160071a001

[38] Lee, C.-Y., Leamy, M.J., Nadler, J.H.: Acoustic absorption calculation in irreducible porous media: A unified computational approach. The Journal of the Acoustical Society of America **126**(4), 1862–1870 (2009) https://doi.org/10.1121/1.3205399

[39] Andrews, G.E., Askey, R., Roy, R.: Special Functions. Encyclopedia of Mathematics and Its Applications, vol. 71. Cambridge University Press, Cambridge; New York (1999)

[40] Press, W.H., Teukolsky, S.A., Vetterling, W.T., Flannery, B.P.: Numerical Recipes in C: The Art of Scientific Computing, 2nd edn. Cambridge University Press, Cambridge (1992)

[41] Sakai, Y., Manhart, M.: Consistent Flow Structure Evolution in Accelerating Flow Through Hexagonal Sphere Pack. Flow, Turbulence and Combustion **105**(2), 581–606 (2020) https://doi.org/10.1007/s10494-020-00168-4

[42] Sakai, Y., Unglehrt, L., Manhart, M.: Similarity of start-up flow in porous media for large pressure gradients. Journal of Fluid Mechanics **1043**, 29

(2026) https://doi.org/10.1017/jfm.2026.12037

[43] Manhart, M., Tremblay, F., Friedrich, R.: MGLET: A parallel code for efficient DNS and LES of complex geometries. In: Jenssen, C.B., Kvamsdal, T., Andersson, H.I., Pettersen, B., Ecer, A., Periaux, J., Satofuka, N., Fox, P. (eds.) Parallel Computational Fluid Dynamics 2000, pp. 449–456. North-Holland, Amsterdam (2001). https://doi.org/10.1016/B978-044450673-3/50123-8

[44] Verstappen, R.W.C.P., Veldman, A.E.P.: Symmetry-preserving discretization of turbulent flow. Journal of Computational Physics **187**(1), 343–368 (2003) https://doi.org/10.1016/S0021-9991(03)00126-8

[45] Williamson, J.H.: Low-storage Runge-Kutta schemes. Journal of Computational Physics **35**(1), 48–56 (1980) https://doi.org/10.1016/0021-9991(80)90033-9

[46] Chorin, A.J.: Numerical solution of the Navier-Stokes equations. Mathematics of Computation **22**(104), 745–762 (1968) https://doi.org/10.1090/S0025-5718-1968-0242392-2

[47] Peller, N.: Numerische Simulation turbulenter Strömungen mit Immersed Boundaries. PhD thesis, Technical University of Munich, Munich (January 2010)

[48] Unglehrt, L., Manhart, M.: Onset of nonlinearity in oscillatory flow through a hexagonal sphere pack. Journal of Fluid Mechanics **944**, 30 (2022) https://doi.org/10.1017/jfm.2022.496

[49] Unglehrt, L., Manhart, M.: Direct and Large–Eddy simulation of turbulent oscillatory flow through a hexagonal sphere pack. In: Marchioli, C., Salvetti, M.V., Garcia-Villalba, M., Schlatter, P. (eds.) Direct and Large Eddy Simulation XIII: Proceedings Of DLES13, 1st edn. ERCOFTAC Series, pp. 118–123. Springer Cham, Cham (2023). https://doi.org/10.1007/978-3-031-47028-8_18

[50] Jacobs, B.A., Laurén, F., Nordström, J.: On the order reduction of approximations of fractional derivatives: An explanation and a cure. BIT Numerical Mathematics **63**(1), 17 (2023) https://doi.org/10.1007/s10543-023-00961-3

[51] van Hinsberg, M.A.T., ten Thije Boonkkamp, J.H.M., Clercx, H.J.H.: An efficient, second order method for the approximation of the Basset history force. Journal of Computational Physics **230**(4), 1465–1478 (2011) https://doi.org/10.1016/j.jcp.2010.11.014